Applied Physics A (2023) 129:38
https://doi.org/10.1007/s00339-022-06320-3

Applied Physics A
Materials Science & Processing

Preparation, characterization and magnetic properties of $Sm_{0.95}Ho_{0.05}FeO_3$ nanoparticles and their application in the purification of water

M. M. Arman[1]

Received: 20 July 2022 / Accepted: 9 December 2022 / Published online: 17 December 2022

Abstract
$Sm_{0.95}Ho_{0.05}FeO_3$ was successfully prepared in a single phase using the citrate combustion method. The investigated sample was characterized using X-ray diffraction (XRD), a high-resolution transmission electron microscope (HRTEM) and X-ray photoemission spectroscopy (XPS). XRD confirmed that the sample was synthesized in an orthorhombic phase with an average crystallite size of 12 nm. HRTEM indicated that the sample was prepared in the nanoscale with an average particle size of 18 nm. XPS was used to identify the chemical bonds, binding energies and core levels of $Sm_{0.95}Ho_{0.05}FeO_3$. The magnetic properties were studied using a vibrating sample magnetometer and DC magnetic susceptibility using Faraday's method. The sample has an antiferromagnetic behavior with weak ferromagnetic components. The presence of magnetic Ho^{3+} ions in the $SmFeO_3$ sample causes the magnetic exchange interaction between the 2*p* orbital of Fe^{3+} and the 4*d* subshell of Ho^{3+} ions. The dependence of pH value on the removal efficiency of Pb^{2+} from water was studied. The maximum Pb^{2+} removal efficiency of the Ho-doped $SmFeO_3$ nano perovskite is 26% at pH = 5 and 99% at pH = 8. The Freundlich, Langmuir and Temkin isotherms were studied to understand the adsorption mechanism. The Temkin adsorption isotherm best fitted with the experimental data.

Keywords $Sm_{0.95}Ho_{0.05}FeO_3$ · Perovskites · The removal efficiency · Nanoparticles

1 Introduction

Rare earth orthoferrite ($RFeO_3$) has attracted attention due to its interesting physical and chemical properties, such as multiferroicity, magnetic properties, spin–phonon coupling, catalytic properties, an abnormal dielectric constant, magnetization reversal at very low temperatures, a high Neel temperature (T_N) above room temperature and a high dielectric constant [1–6]. Many applications for ABO_3 orthoferrites have been developed, including energy storage devices, spintronics, heavy metal and dye removal from wastewater, and chemical sensors [7–11]. Rare earth orthoferrites usually have a distorted orthorhombic structure with the Pbnm space group [6, 8, 12]. In this structure, the rare earth cation R^{3+} has 12 coordination numbers, while Fe ions coordinate with six O^{2-} anions, forming FeO_6 octahedra [13, 14]. The tilting and distortion of FeO_6 affect the ionic radii of rare earth cations. The distortion of FeO_6 increases by decreasing the rare earth ionic radii due to the R–O bond length and bond angle change.

$SmFeO_3$ is one of the rare earth orthoferrite materials. It has attracted great attention from researchers due to its properties, such as the antiferromagnetic properties with weak ferromagnetism, the highest spin reorientation transition temperature (470 K), the particle size-affected dielectric constant and piezoelectricity at room temperature [14]. The magnetic properties of $SmFeO_3$ originate from three magnetic interactions, i.e., rare earth–rare earth (R^{3+}–R^{3+}), rare earth–iron (R^{3+}–Fe^{3+}) and iron–iron (Fe^{3+}–Fe^{3+}) interactions [1, 15].

The change in A-site cation radius affects the distortion of the perovskite structure and the tilting of the FeO_6 octahedron. The doping of rare earth ions at the A site has an impact on the magnetic properties of $SmFeO_3$. Liu [16] studied the effect of nonmagnetic La ion doping on the magnetic properties of $SmFeO_3$. Because the Sm spins are

✉ M. M. Arman
mmarmsci@gmail.com; mmarmsci@cu.edu.eg

[1] Materials Science Lab (1), Physics Department, Faculty of Science, Cairo University, Giza, Egypt

in a frustrated state, the magnetic anisotropy energy and exchange bias of $Sm_{1-x}La_xFeO_3$ rise slightly for $x=0.05$ and then fall by increasing the La content by more than 0.05. Praveena et al. [15] prepared $Sm_{1-x}Ca_xFeO_3$ where $x=0$, 0.25, 0.5, 0.75 and 1 using the sol–gel method at low temperatures. As Ca^{2+} increases, a significant enhancement in remnant magnetization (M_r) and coercivity (H_c) is observed. The magnetic properties of the $Sm_{1-x}Ca_xFeO_3$ samples were improved due to the destruction of the spin cycloid with Sm.

Heavy metal pollution is an international issue that is growing with the development of modern industry. The sources of lead in the environment are ceramic printing industries, battery manufacturing, ammunition and acid metal plating [17]. The presence of the toxic heavy metal lead in water has great harmful effects on the human body, so it is one of the most worrying problems [18, 19]. High lead exposure has been reported to have a number of negative health impacts on children, including neurotoxicity [20], low IQ [21, 22], poor mental development [23], low quantitative skills [24], and learning difficulties. For adults, lead exposure has health consequences such as diabetes, renal disease [25] and cognitive dysfunction from early childhood exposure [26].

There are many conventional methods for the removal of heavy metal ions, such as membrane filtration, chemical precipitation, reverse osmosis, ultrafiltration and flotation. The adsorption method is more effective for heavy metal ion removal due to its properties such as simplicity, cost-effectiveness, no sludge formation and good regeneration capacity [27–29]. Adsorption occurs due to the physical or chemical attraction of lead ions to the surface of the adsorbent [30].

Perovskites are effective materials for heavy metal removal owing to their properties such as high stability, low price, high surface energy, and absorptivity, catalytic, electronic, magnetic and optical characteristics [28]. One of the main advantages of using magnetic materials (i.e., perovskite) for heavy metal removal is the easy separation from the solution by an external magnet. Some of the perovskite samples that were used for heavy metal removal are $La_{0.85}Ce_{0.15}FeO_3$ [8], $CeCoO_3$ [31], $LaFeO_3$ [32], and $LaAlO_3$ [33]. Meanwhile, the removal of lead ions from water by using $Sm_{0.95}Ho_{0.05}FeO_3$ nanocomposites has not been reported yet. Therefore, this work demonstrated the use of Ho-doped $SmFeO_3$ nanoparticles to eliminate lead from aqueous solutions.

In this work, $Sm_{0.95}Ho_{0.05}FeO_3$ was synthesized using a simple citrate combustion method. The aim of this study is to study the phase formation, morphology and magnetic behavior of $Sm_{0.95}Ho_{0.05}FeO_3$. The other goal is to examine the ability of the investigated sample to remove lead from water. The effect of pH value on the removal efficiency of pb^{2+} ions from water was studied.

2 Experimental work

2.1 Preparation of nanocomposites

$Sm_{0.95}Ho_{0.05}FeO_3$ was synthesized by the citrate combustion method. The precursor metal nitrates (purity 99.9% Sigma-Aldrich) were mixed in stoichiometric ratios with citric acid as a fuel. The citric acid/nitrate ratio is equal to 1. The pH of the solution was adjusted to 7 using the ammonia solution. The solution was heated on the hot plate until a highly viscous liquid was formed. The viscous liquid swelled and auto-ignited as it was heated further, resulting in a fluffy powder. This preparation method is low cost, simple, and quick. The sample was ground well for 1 h using an agate mortar to obtain a powder. The sample was sintered at 500 °C for 2 h with a heating/cooling rate of 4 degrees/min in air. Figure 1 illustrates the flowchart of the preparation of Ho-doped $SmFeO_3$.

2.2 Sample characterizations and measurements

The sample was well ground into powder before being subjected to the following characterizations. X-ray diffraction (XRD, Bruker advance D8 diffractometer, $\lambda=1.5418$ Å) was used to study the structure of the investigated sample, $Sm_{0.95}Ho_{0.05}FeO_3$. The crystalline phases of the sample were identified using the International Centre for Diffraction Data (ICDD) card number 74-1474.

A certain amount of the sample was suspended in deionized water by using an ultrasonicator for 30 min before the characterization using HRTEM. The surface morphology of Ho-doped $SmFeO_3$ was characterized using a transmission electron microscope (HRTEM, JEOL-2100) operated at 200 kV. The surface chemical composition of the investigated sample was measured using the X-ray photoelectron spectrometer (XPS) via K-ALPHA (Thermo Fisher Scientific, USA).

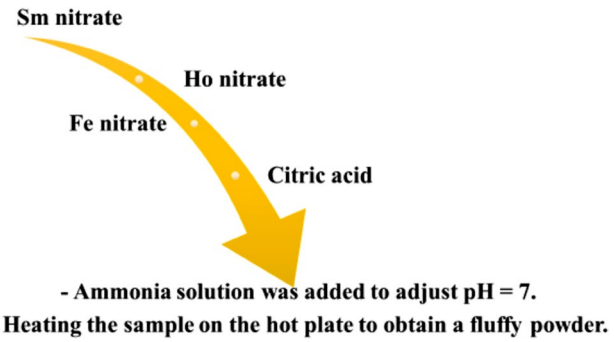

Fig. 1 Flowchart for the preparation of $Sm_{0.95}Ho_{0.05}FeO_3$

The magnetic behavior of the Ho-doped perovskite $SmFeO_3$ was studied using a vibrating sample magnetometer and DC magnetic susceptibility using the Faraday method [34]. The magnetic susceptibility of the investigated sample was measured by introducing a cylindrical glass tube with a small amount of powdered sample at the point of maximum gradient.

2.3 Heavy metal removal

2.3.1 Effect of pH value

A lead ion solution of concentration (100 ppm) was prepared from pure lead nitrate to determine the heavy metal ion removal efficiency of the $Sm_{0.95}Ho_{0.05}FeO_3$ sample. A working solution (50 ppm) was prepared by diluting the above solution. A few 250-mL flasks containing 50 ppm lead ion solution and 0.02 g of the investigated sample were used. By using ammonia and diluted nitric acid solutions, the pH values of lead solutions were adjusted from 3 to 8. The resultant solutions were stirred at 25 °C using an electric shaker (Orbital Shaker SO1) at 200 rpm for 1 h. By using a 0.2-µm syringe filter, 10 mL of the supernatant solutions was filtered. Inductively coupled plasma spectrometry (ICP, Prodigy7) was used to calculate the concentration of pb^{2+} ions in the filtrated solution.

The metal ion removal efficiency (η) and the equilibrium adsorption capacity (q) were calculated according to the following equations [35]:

$$\eta = \frac{C_i - C_e}{C_i} \times 100, \tag{1}$$

$$q = \frac{(C_i - C_e)V}{m}, \tag{2}$$

where C_i and C_e are the initial and final concentrations (mg/L) of the metal ion solution, respectively, while m is the mass of the adsorbent and V is the volume of Pb (II) solution.

3 Results and discussion

XRD was used to examine the crystalline structure of the prepared sample, $Sm_{0.95}Ho_{0.05}FeO_3$. Figure 2 shows the XRD pattern of the investigated sample. All the diffraction peaks are indexed with the ICCD card number 74-1474. $Sm_{0.95}Ho_{0.05}FeO_3$ has been synthesized in a single-phase orthorhombic structure with space group Pbnm. Major diffracted peaks (110), (111), (112), (220), (131), (312), (133) and (224) were observed in the XRD pattern at 2θ values of 22.96, 25.66, 32.51, 47.05, 53.38, 58.88, 63.97 and 69.88,

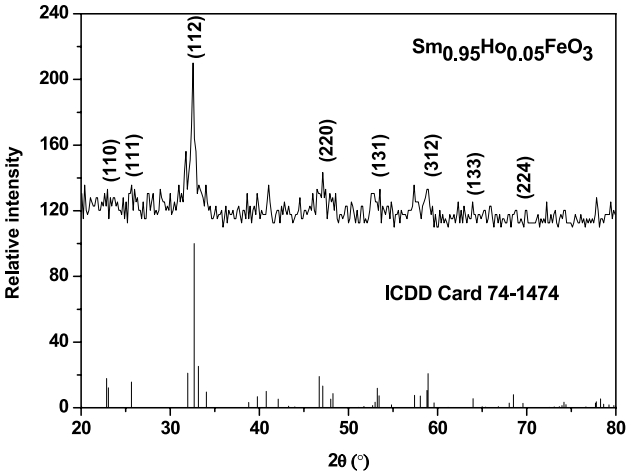

Fig. 2 XRD of the sample $Sm_{0.95}Ho_{0.05}FeO_3$

which indicates the sample has an orthorhombic phase. The high-intensity peak (112) observed at 2θ indicates the growth direction of $Sm_{0.95}Ho_{0.05}FeO_3$. The values of lattice parameters were calculated on the basis of the orthorhombic structure according to the following equation:

$$\frac{1}{d^2} = \frac{h^2}{a^2} + \frac{k^2}{b^2} + \frac{l^2}{c^2}. \tag{3}$$

The average crystallite size was estimated using Scherer's equation [36] and is reported in Table 1. The value of the crystallite size (12.1 nm) indicates that the sample was synthesized in the nano scale.

$$D = \frac{0.94\lambda}{\beta \cos\theta}. \tag{4}$$

The theoretical density of the investigated sample was calculated using the following equation:

$$D_x = \frac{ZM}{NV}, \tag{5}$$

where $Z=4$ is the number of molecules per unit cell, N is Avogadro's number, M is the molecular weight, and V is the unit cell volume.

The Goldsmith perovskite tolerance factor (t) measures the lattice mismatch between the ions of the perovskite materials [37]. The highest value of t is equal to 1 for a cubic perovskite structure. The value of the tolerance factor was calculated according to the following equation:

$$t = \frac{r_A + r_O}{\sqrt{2}(r_{Fe} + r_O)}, \tag{6}$$

Table 1 Experimental lattice parameters: crystallite size (D), unit cell volume (V), theoretical density (D_x) and tolerance factor (t)

Sample	(a) Å	(b) Å	(c) Å	D (nm)	V (Å)^3	D_x (g cm^{-3})	t
$Sm_{0.95}Ho_{0.05}FeO_3$	5.397	5.606	7.739	12.1	234.1	7.230	0.8786

where r_A, r_B, and r_O are the ionic radii of the A, B, and oxygen ions, respectively. The A-site ionic radius can be calculated according to the equation $r_A = 0.95r_{Sm}^{3+} + 0.05r_{Ho}^{3+}$. The tolerance factor value of the investigated sample is 0.8786, which indicates that the sample has an orthorhombic structure. The tolerance factor is less than one due to the lattice distortion arising from the tilting of <FeO_6> octahedral structure.

Figure 3 illustrates the EDX energy spectra of $Sm_{0.95}Ho_{0.05}FeO_3$. The atomic percentages (at%) and weight percentages (wt%) of the Fe, O, Sm, and Ho elements are illustrated in the inset table in Fig. 3. The experimental at% and wt% were obtained from EDX, while the theoretical values were calculated from the chemical formula $Sm_{0.95}Ho_{0.05}FeO_3$. The small variation of weight and atomic percentages between the experimental and theoretical values is due to oxygen deficiency, which can be advantageous for heavy metal removal from water.

Figure 4a, b illustrates the HRTEM images of the investigated nanoparticles at different scales. The average particle size of $Sm_{0.95}Ho_{0.05}FeO_3$ is 18 nm, which confirms that the sample was synthesized in the nanoscale. The nanoparticles are agglomerated due to the magnetic properties of the sample. Figure 4b includes an inset of the selected area electron diffraction (SAED) pattern. The bright rings in the SAED indicate that the sample was synthesized in good crystalline form. The SAED pattern also illustrated that the prepared $Sm_{0.95}Ho_{0.05}FeO_3$ nanoparticles are polycrystalline in nature.

The XPS characterization was carried out to verify the chemical composition and valence state of the $Sm_{0.95}Ho_{0.05}FeO_3$ nanoparticles. The wide-range XPS survey spectra of $Sm_{0.95}Ho_{0.05}FeO_3$ nanoparticles are illustrated in Fig. 5a. The peaks of different elements such as Sm, Ho, Fe, O, and C have been identified. The C 1s peak is observed at 287.21 eV, which is used as a charge reference to rectify the binding energy of the XPS spectra [38]. Figure 5a illustrates that there is no secondary phase from holmium metal or oxide. Therefore, Ho was substituted at the expense of the Sm site and maintained the perovskite structure in a single phase as a result obtained from XRD data. The XPS peak of Ho 4d at a binding energy of 160.79 eV due to the presence of Ho^{3+} is shown in Fig. 5b [39–41]. The Ho 4d spectrum is obvious in a small range of scan spectra as a result of the very small quantity of Ho in $Sm_{0.95}Ho_{0.05}FeO_3$ perovskite.

The magnetic parameters of orthoferrite depend on many factors, such as the composition, the cation preference occupation, purity, homogeneity and surface to volume ratio [1]. The magnetic properties of $Sm_{0.95}Ho_{0.05}FeO_3$ were studied by using the hysteresis loop and Faraday's law. The magnetic hysteresis loop of the investigated perovskite is illustrated in Fig. 6 at room temperature. The values of the maximum magnetization (M_s), the coercive field (H_c) and the remnant magnetization (M_r)

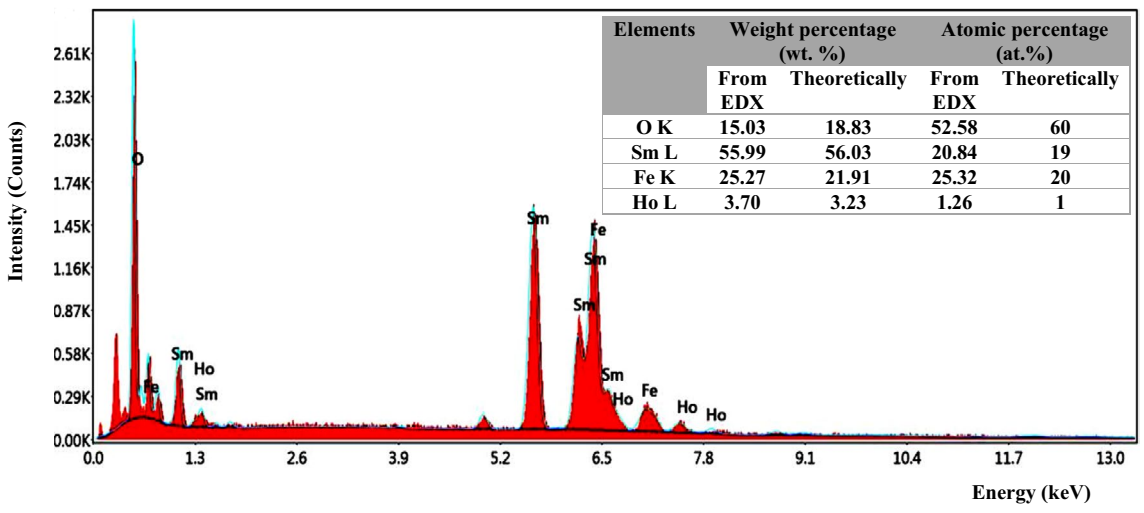

Fig. 3 EDX for the $Sm_{0.95}Ho_{0.05}FeO_3$ sample. The inset table shows the weight percentage (wt%) and atomic percentage (at%) of the elements O, Sm, Fe, and Ho

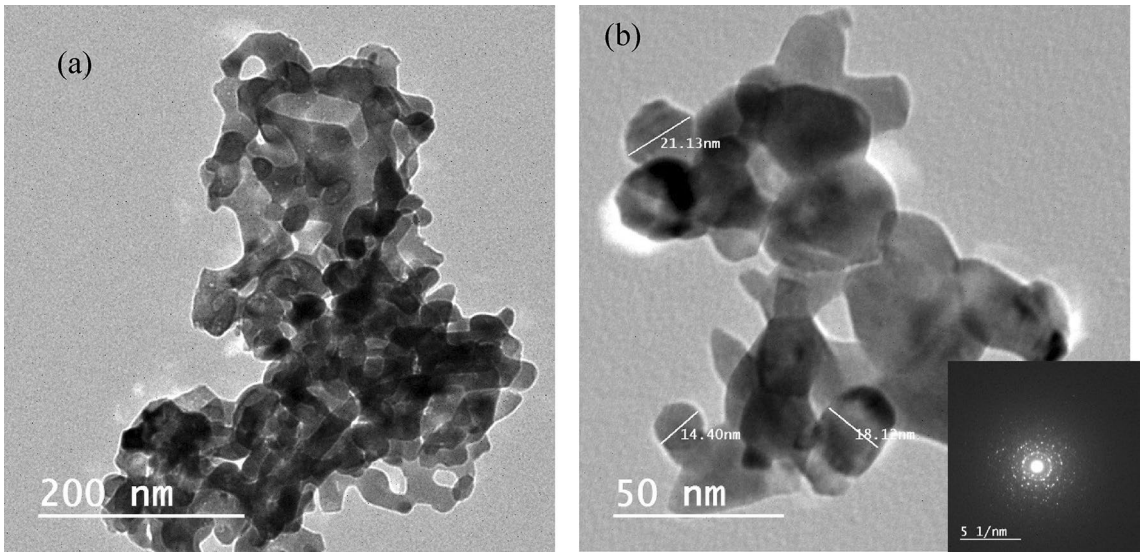

Fig. 4 HRTEM of the sample $Sm_{0.95}Ho_{0.05}FeO_3$

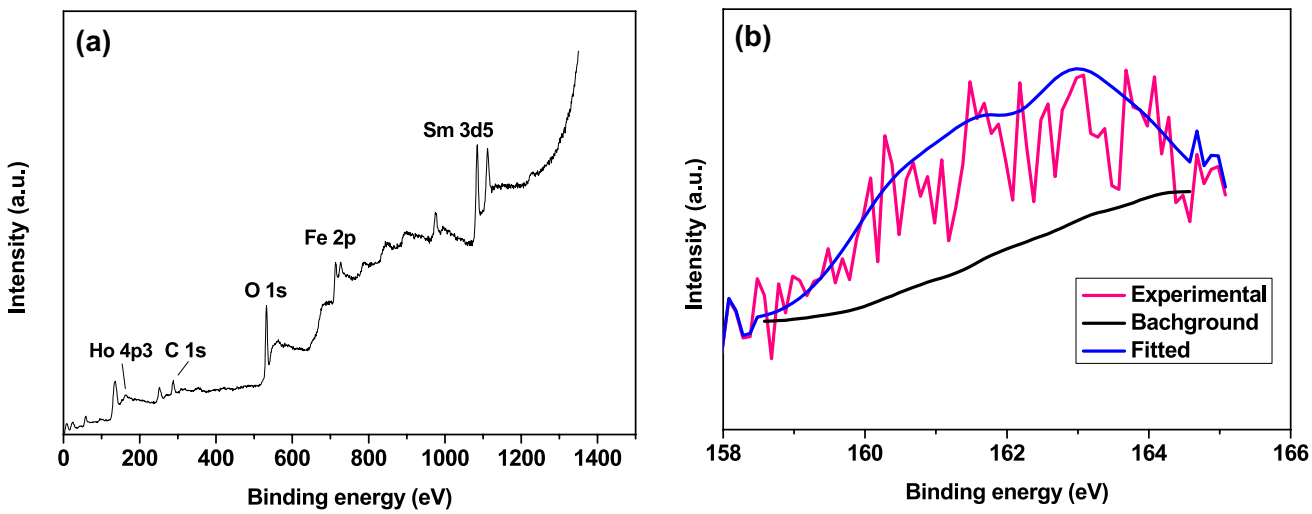

Fig. 5 XPS spectra of $Sm_{0.95}Ho_{0.05}FeO_3$: **a** a wide scan and **b** narrow scans of Ho 4*d* signals

are listed in Table 2. The hysteresis loop has a small area with nonlinearity, a very small coercive field, and remnant magnetization. The non-saturation behavior of the magnetic loop shows the dominance of its antiferromagnetic character. The hysteresis loop has *S*-shape, which indicates the presence of an antiferromagnetic order with weak ferromagnetic components [1]. The super exchange interactions are presented between the magnetic ions Fe^{3+}, Ho^{3+} and Sm^{3+} ions, while the weak ferromagnetism originates from canted antiferromagnetic spins in the investigated sample. The anisotropy constant value is calculated from the following equation [42] and reported in Table 2.

$$K = \frac{H_C \times M_S}{0.96}, \tag{7}$$

where H_c is the coercivity, K is the magnetic anisotropy constant and M_s denotes saturation magnetization. The weak anisotropy of $Sm_{0.95}Ho_{0.05}FeO_3$ is due to the non-collinearity (canting) of spins on their surface [42].

Ateia et al. [14] used the citrate auto-combustion method to prepare $SmFeO_3$ and found that the saturation magnetization was 0.639 emu/g. In the present study, the maximum magnetization of Ho-doped $SmFeO_3$ increased four times that of $SmFeO_3$ as a result of the substitution of Ho^{3+} ions (10.3 μ_B) instead of Sm^{3+} ions (1.6 μ_B) [43]. Due to lattice distortion

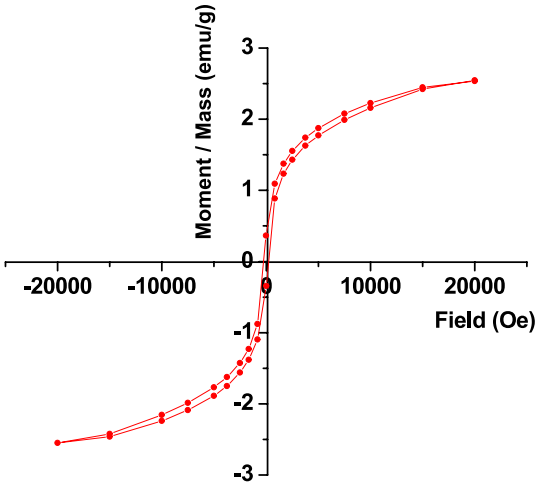

Fig. 6 Room temperature M–H loops of the investigated sample at room temperature

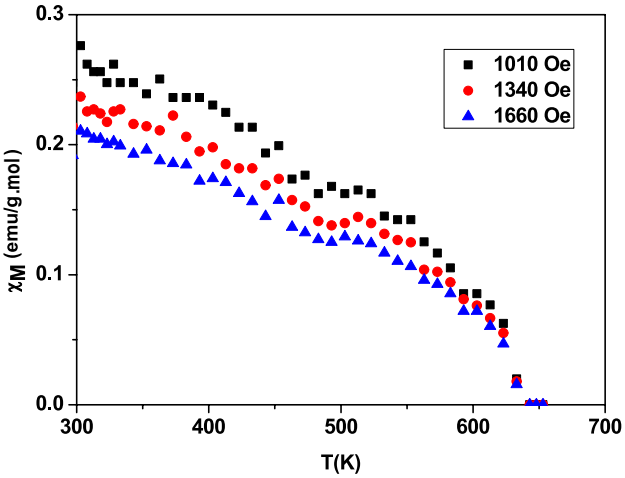

Fig. 7 The dependence of the molar magnetic susceptibility on the absolute temperature for $Sm_{0.95}Ho_{0.05}FeO_3$ at different magnetic field intensities

caused by the difference in ionic radii of Ho^{3+} (1.015 Å) and Sm^{3+} (1.079 Å), the magnetization of $SmFeO_3$ is increased by substituting Ho^{3+} ions for Sm^{3+} ions [44].

The dependence of the molar magnetic susceptibility (χ_M) on the absolute temperature T (K) is illustrated in Fig. 7 for the investigated sample $Sm_{0.95}Ho_{0.05}FeO_3$. The χ_M values decrease as the temperature increases to the Néel temperature. Figure 7 confirms the AFM behavior of the Ho-doped $SmFeO_3$ sample with weak ferromagnetic components [45, 46]. The values of magnetic constants such as Curie temperature (T_c), Curie–Weiss constant (θ), Curie constant (C) and the effective magnetic moment (μ_{eff}) are calculated and reported in Table 3. Introducing the Ho^{3+} ions into the sample increases the magnetization due to the presence of new magnetic interactions between Ho^{3+}–Ho^{3+} and Ho^{3+}–Sm^{3+} interactions. By introducing Ho^{3+} ions into $SmFeO_3$, the distortion increased, as illustrated in the tolerance factor, leading to changes in the bond lengths of Fe–O and Sm–O. The structure distortion, the bond angle and the bond length all strongly affect the super exchange interaction [47]. The presence of magnetic Ho^{3+} ions in the investigated sample causes the magnetic exchange interaction between the 2*p* orbital of Fe^{3+} and the 4*d* sub-shell of Ho^{3+} ions [48].

The interaction between the adsorbent and the adsorbate depends on many factors, such as the pH value of the solution [8]. The pH value determines the adsorbent's net surface charge, the type of adsorbed species and the degree of ionization [49]. In aqueous solutions, iron oxides are hydrated and form FeOH groups, which cover their surfaces. Depending on the pH value of the solution, the hydroxylated sites on the surface can react with H^+ or OH^- ions from dissolved acids or bases, and positive ($FeOH_2^+$) or negative (FeO^-) charges are produced on the surface of perovskite [17].

$$FeOH + OH^- = FeO^- + H_2O,$$
$$FeOH + H^+ = FeOH_2^+.$$

Figure 8 shows the dependence of the adsorption efficiency of the removal of Pb^{2+} heavy metal ions on the pH solution. Since there are more H^+ ions in the solution when the pH is very low, H^+ and heavy metal ions compete for the same active sites on the adsorbent, which results in a low removal efficiency. As pH rises, the sample surface acquires

Table 3 Calculated magnetic constants: Curie temperature (T_c), Curie constant (C), Curie–Weiss constant (θ) and the effective magnetic moment (μ_{eff})

Field (Oe)	T_c (K)	θ (K)	C (emu mole K/g)	μ_{eff} (BM)
1010	635	570	2.407	4.39
1340	635	561	3.29	5.13
1660	635	543	6.44	6.44

Table 2 The values of the maximum magnetization (M_m), remanence magnetization (M_r), the coercive field (H_c), anisotropy constant (K), M–H loop area and squareness ratio for $Sm_{0.95}Ho_{0.05}FeO_3$

Sample	M_m (emu g^{-1})	M_r (emu g^{-1})	H_c Oe	M–H loop area (erg g^{-1})×10^3	K (emu Oe g^{-1})	Squareness
$Sm_{0.95}Ho_{0.05}FeO_3$	2.5467	0.3547	239.35	2323.9	634.95	0.1393

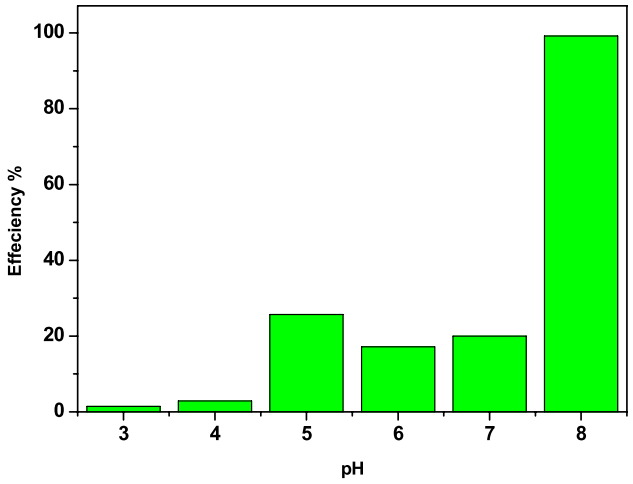

Fig. 8 Effect of pH on the adsorption efficiency of Pb^{2+} ions

a negative sign and the adsorption of lead ions increases. In this case, electrostatic interactions dominate the adsorption process. Figure 8 illustrates that the optimum pH value for precipitate Pb^{2+} is pH = 5. At a high pH value (pH = 8), Pb^{2+} ions precipitate as hydroxide, which is unfavorable for the adsorption process [50].

The adsorption isotherm gives more information about the mechanism of adsorption between the investigated sample and the lead ion liquid phase. In the present work, Langmuir, Freundlich and Temkin isotherm models were studied for the absorption efficiency of lead ions on $Sm_{0.95}Ho_{0.05}FeO_3$.

The Langmuir, Freundlich and Temkin isotherm models [51, 52] were applied to explain the equilibrium adsorption of the pb^{2+} ion on $Sm_{0.95}Ho_{0.05}FeO_3$ nanoparticles. Equations (8)–(10) express the Langmuir, Freundlich and Temkin isotherm models, respectively.

$$\frac{C_e}{q_e} = \frac{1}{q_m K_L} + \frac{C_e}{q_m}, \tag{8}$$

$$q_e = K_f C_e^{\frac{1}{n}}, \tag{9}$$

$$q_e = \frac{RT}{b_T} \ln K_T + \frac{RT}{b_T} \ln C_e, \tag{10}$$

where C_e is the equilibrium metal concentration (mg/L), q_m and K_L are the Langmuir constants associated with maximum adsorption capacity (mg/g), K_f is the Freundlich constant, $\frac{1}{n}$ is the adsorption intensity, T is the absolute temperature (K), R is the common gas constant (0.008314 kJ/mol K), $\frac{1}{b_T}$ is the Temkin constant related to the heat of sorption (kJ/mol) and K_T is the Temkin constant related to adsorption capacity (L/g).

Figure 9 illustrates the relationship between ln q_e and ln C_e which agrees with the Freundlich isotherm model. The values of $1/n$ and K_f were calculated from the slope and the intercept of the best fit line in Fig. 9. The dependence of C_e/q on C_e according to the Langmuir isotherm model is illustrated in Fig. 10. Adsorbent–adsorbate interactions are taken into account in the Temkin isotherm. Figure 11 illustrates the linear plot between q_e and lnC_e according to the Temkin isotherm model. The constants $\frac{1}{b_T}$ and K_T can be determined from the slope and intercept, respectively.

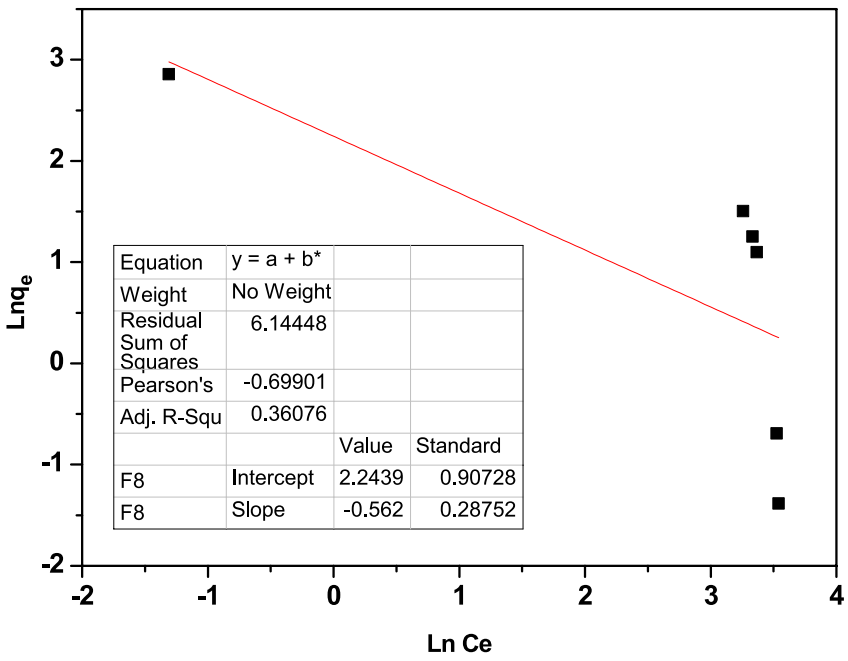

Fig. 9 Linear fit of experimental data of the adsorption of Pb^{2+} according to the Freundlich isotherm model

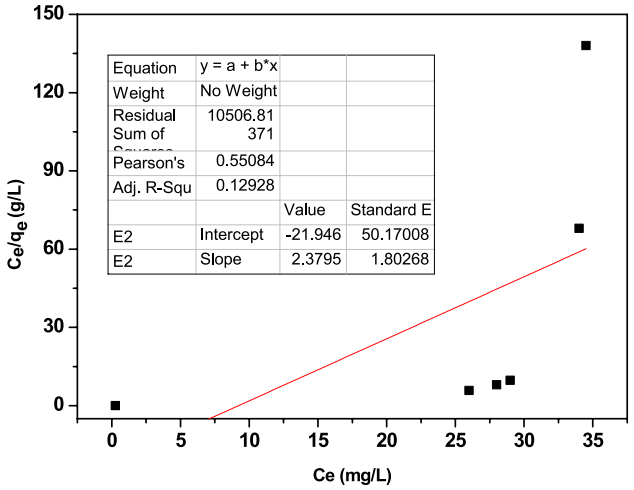

Fig. 10 Linear fit of experimental data of the adsorption of Pb^{2+} using the Langmuir adsorption isotherm model

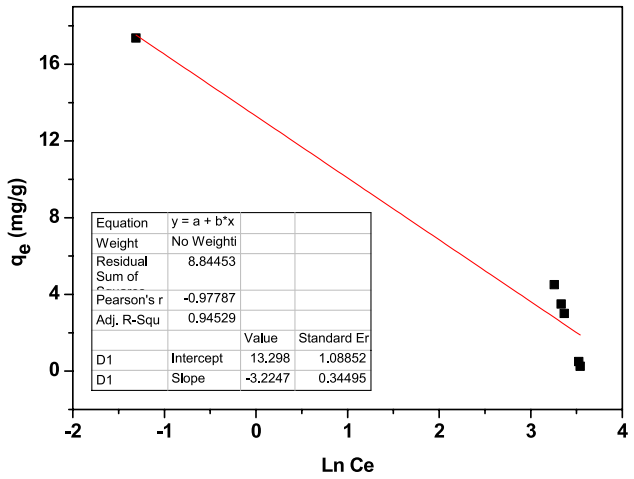

Fig. 11 Temkin adsorption isotherm model of the adsorption of Pb^{2+} on $Sm_{0.95}Ho_{0.05}FeO_3$ nanoparticles

Table 4 The correlation coefficient (R^2) of different isotherm models

	Freundlich isotherm	Langmuir isotherm	Temkin isotherm
R^2	0.3607	0.1292	0.9453

Table 4 shows the values of the correlation coefficient (R^2) for the Langmuir, Freundlich and Temkin isotherm models. The Temkin isotherm has an R^2 of 0.9453. Thus, the Temkin adsorption isotherm best fitted with the experimental data.

4 Conclusions

The X-ray diffraction analysis ensures $Sm_{0.95}Ho_{0.05}FeO_3$ was synthesized in a single-phase orthorhombic structure. The average particle size of the investigated sample is 18 nm. The bright rings in the SAED indicate that the sample was synthesized with good crystalline nature. XPS illustrated that Ho was substituted at the expense of Sm and maintained the perovskite structure in a single phase. $Sm_{0.95}Ho_{0.05}FeO_3$ has antiferromagnetic properties with a maximum magnetization equal to 2.5467 emu g^{-1}. Introducing the Ho^{3+} ions into the sample increases the magnetization due to the presence of new magnetic interactions between Ho^{3+}–Ho^{3+} and Ho^{3+}–Sm^{3+} interactions. Ho-doped $SmFeO_3$ can act as a heavy metal pb^{2+} adsorber from wastewater. The optimum removal efficiency of lead ions from water is 26% by $Sm_{0.95}Ho_{0.05}FeO_3$. The Temkin adsorption isotherm is the best description of the adsorption of the Pb^{2+} ion from water.

Funding Open access funding provided by The Science, Technology & Innovation Funding Authority (STDF) in cooperation with The Egyptian Knowledge Bank (EKB).

Declarations

Conflict of interest The author declares no conflict of interest regarding the publication of this paper.

References

1. R. Shukla, R. Dhaka, S. Dash, S.C. Sahoo, B. Bahera, P.D. Babu, R. Choudhary, A.K. Patra, Structural, dielectric and magnetic properties of Bi–Mn doped $SmFeO_3$. Ceram. Int. **46**(7), 8730–8744 (2020)
2. Z. Cheng, F. Hong, Y. Wang, K. Ozawa, H. Fujii, H. Kimura, Y. Du, X. Wang, S. Dou, Interface strain-induced multiferroicity in a $SmFeO_3$ film. ACS Appl. Mater. Interfaces **6**(10), 7356–7362 (2014)
3. A.V. Kimel, A. Kirilyuk, A. Tsvetkov, R.V. Pisarev, T. Rasing, Laser-induced ultrafast spin reorientation in the antiferromagnet $TmFeO_3$. Nature **429**(6994), 850–853 (2004)

4. M.M. Arman, M.A. Ahmed, Effects of vacancy co-doping on the structure, magnetic and dielectric properties of $LaFeO_3$ perovskite nanoparticles. Appl. Phys. A **128**(7), 1–9 (2022)
5. M. Reda, S.I. El-Dek, M.M. Arman, Improvement of ferroelectric properties via Zr doping in barium titanate nanoparticles. J. Mater. Sci.: Mater. Electron. **33**, 1–24 (2022)
6. S. Chaturvedi, P. Shyam, A. Apte, J. Kumar, A. Bhattacharyya, A.M. Awasthi, S. Kulkarni, Dynamics of electron density, spin-phonon coupling, and dielectric properties of $SmFeO_3$ nanoparticles at the spin-reorientation temperature: role of exchange striction. Phys. Rev. B **93**(17), 174117 (2016)
7. J.T. Mefford, W.G. Hardin, S. Dai, K.P. Johnston, K.J. Stevenson, Anion charge storage through oxygen intercalation in $LaMnO_3$ perovskite pseudocapacitor electrodes. Nat. Mater. **13**(7), 726–732 (2014)
8. M.M. Arman, Synthesis, characterization, magnetic properties, and applications of $La_{0.85}Ce_{0.15}FeO_3$ perovskite in heavy metal Pb^{2+} removal. J. Supercond. Novel Magn. **2022**, 1–9 (2022)
9. Z.A. Elsiddig, H. Xu, D. Wang, W. Zhang, X. Guo, Y. Zhang, Z. Sun, J. Chen, Modulating Mn^{4+} ions and oxygen vacancies in nonstoichiometric $LaMnO_3$ perovskite by a facile sol–gel method as high-performance supercapacitor electrodes. Electrochim. Acta **253**, 422–429 (2017)
10. Z. Anajafi, M. Naseri, G. Neri, Acetone sensing behavior of *p*-$SmFeO_3$/*n*-ZnO nanocomposite synthesized by thermal treatment method. Sens. Actuators B Chem. **304**, 127252 (2020)
11. P. Song, H. Zhang, D. Han, J. Li, Z. Yang, Q. Wang, Preparation of biomorphic porous $LaFeO_3$ by sorghum straw biotemplate method and its acetone sensing properties. Sens. Actuators B Chem. **196**, 140–146 (2014)
12. M.M. Arman, N.G. Imam, R.L. Portales, S.I. El-Dek, Synchrotron radiation X-ray absorption fine structure and magnetization improvement of A-site Ce^{3+} doped $LaFeO_3$. J. Magn. Magn. Mater. **513**, 167097 (2020)
13. M.M. Arman, M.A. Ahmed, S.I. El-Dek, Influence of vacancy co-doping on the physical features of $NdFeO_3$ nanostructure perovskites. Appl. Phys. A **126**(1), 1–10 (2020)
14. E.E. Ateia, M.M. Arman, E. Badawy, Role of coupling divalent cations on the physical properties of $SmFeO_3$ prepared by citrate auto-combustion technique. Appl. Phys. A **125**(8), 1–7 (2019)
15. K. Praveena, P. Bharathi, H.L. Liu, K.B.R. Varma, Structural, multiferroic properties and enhanced magnetoelectric coupling in $Sm_{1-x}CaxFeO_3$. Ceram. Int. **42**(12), 13572–13585 (2016)
16. Q. Liu, X.X. Wang, C. Song, J.X. Sui, X. Yan, J.C. Zhang, H.S. Zhao, F. Yuan, Y.Z. Long, Magnetic properties of La doped $SmFeO_3$. J. Magn. Magn. Mater. **469**, 76–80 (2019)
17. M.A. Ahmed, S.M. Ali, S.I. El-Dek, A. Galal, Magnetite–hematite nanoparticles prepared by green methods for heavy metal ions removal from water. Mater. Sci. Eng. B **178**(10), 744–751 (2013)
18. B. Daus, R. Wennrich, H. Weiss, Sorption materials for arsenic removal from water: a comparative study. Water Res. **38**(12), 2948–2954 (2004)
19. R. Bondu, V. Cloutier, E. Rosa, M. Benzaazoua, A review and evaluation of the impacts of climate change on geogenic arsenic in groundwater from fractured bedrock aquifers. Water Air Soil Pollut. **227**(9), 1–14 (2016)
20. H.L. Needleman, C. McFarland, R.B. Ness, S.E. Fienberg, M.J. Tobin, Bone lead levels in adjudicated delinquents: a case control study. Neurotoxicol. Teratol. **24**(6), 711–717 (2002)
21. H.W. Mielke, J.L. Adams, P.L. Reagan, P.W. Mielke Jr., Soil-dust lead and childhood lead exposure as a function of city size and community traffic flow: the case for lead abatement in Minnesota. Environ. Geochem. Health **9**, 253–271 (1989)
22. H.W. Mielke, Lead dust contaminated USA communities: comparison of Louisiana and Minnesota. Appl. Geochem. **8**, 257–261 (1993)
23. L. Agwaramgbo, E. Agwaramgbo, C. Mercadel, S. Edwards, E. Buckles, Lead remediation of contaminated water by charcoal, LA red clay, spinach, and mustard green. J. Environ. Prot. **2**(9), 1240 (2011)
24. R.L. Canfield, C.R. Henderson Jr., D.A. Cory-Slechta, C. Cox, T.A. Jusko, B.P. Lanphear, Intellectual impairment in children with blood lead concentrations below 10 μg per deciliter. N. Engl. J. Med. **348**(16), 1517–1526 (2003)
25. J.L. Lin, D.T. Lin-Tan, K.H. Hsu, C.C. Yu, Environmental lead exposure and progression of chronic renal diseases in patients without diabetes. N. Engl. J. Med. **348**(4), 277–286 (2003)
26. R.A. Shih, H. Hu, M.G. Weisskopf, B.S. Schwartz, Cumulative lead dose and cognitive function in adults: a review of studies that measured both blood lead and bone lead. Environ. Health Perspect. **115**(3), 483–492 (2007)
27. J. Rubio, M.L. Souza, R.W. Smith, Overview of flotation as a wastewater treatment technique. Miner. Eng. **15**(3), 139–155 (2002)
28. G. Jayanthi, S. Sumathi, V. Andal, Synthesis and applications of perovskite in heavy metal ions removal—a brief perspective. Mater. Today Proc. **55**, 201–211 (2022)
29. M. Czikkely, E. Neubauer, I. Fekete, P. Ymeri, C. Fogarassy, Review of heavy metal adsorption processes by several organic matters from wastewaters. Water **10**(10), 1377 (2018)
30. M.I. Sabela, K. Kunene, S. Kanchi, N.M. Xhakaza, A. Bathinapatla, P. Mdluli, D. Sharma, K. Bisetty, Removal of copper(II) from wastewater using green vegetable waste derived activated carbon: an approach to equilibrium and kinetic study. Arab. J. Chem. **12**(8), 4331–4339 (2019)
31. C.B. Njoku, E. Oseghe, T.A. Msagati, Synthesis and application of perovskite nanoparticles for the adsorption of ketoprofen and fenoprofen in wastewater for sustainable water management. J. Mol. Liq. **346**, 118232 (2022)
32. M.P. Rao, S. Musthafa, J.J. Wu, S. Anandan, Facile synthesis of perovskite $LaFeO_3$ ferroelectric nanostructures for heavy metal ion removal applications. Mater. Chem. Phys. **232**, 200–204 (2019)
33. W. Haron, A. Wisitsoraat, U. Sirimahachai, S. Wongnawa, Removal of toxic heavy metal ions from water with $LaAlO_3$ perovskite. Songklanakarin J. Sci. Technol. **40**(5), 993–1001 (2018)
34. A. Rais, Absolute method of calibration of a Faraday microbalance. Measurement **35**(3), 289–292 (2004)
35. R. Ramadan, S.I. El-Dek, M.M. Arman, Enhancement of Mn-doped magnetite by mesoporous silica for technological application. Appl. Phys. A **126**(11), 1–13 (2020)
36. M.M. Arman, Structural, morphological and magnetic properties of hexaferrite $BaCo_2Fe_{16}O_{27}$ nanoparticles and their efficient lead removal from water. Appl. Phys. A **128**(12), 1–10 (2022)
37. M.M. Arman, S.I. El-Dek, Role of annealing temperature in tailoring Ce-doped $LaFeO_3$ features. J. Phys. Chem. Solids **152**, 109980 (2021)
38. P.W. Wang, M. Guttag, C.-S. Tu, Surface modification of multiferroic $BiFeO_3$ ceramic by argon sputtering. J. Surf. Eng. Mater. Adv. Technol. **4**, 295–308 (2014)
39. S.K. Ray, Y.K. Kshetri, T. Yamaguchi, T.H. Kim, S.W. Lee, Characterization and multicolor upconversion emission properties of $BaMoO_4$: Yb^{3+}, Ln^{3+} (Ln = Tm, Ho, Tm/Ho) microcrystals. J. Solid State Chem. **272**, 87–95 (2019)
40. T. Han, S. Ma, P. Yun, H. Sheng, X. Xu, P. Cao, S. Pei, A. Alhadi, Synthesis and characterization of Ho-doped $SmFeO_3$ nanofibers with enhanced glycol sensing properties. Vacuum **191**, 110378 (2021)
41. A. Manzoor, M.A. Khan, T. Alshahrani, M.H. Alhossainy, M. Sharif, T. Munir, M.I. Arshad, M.A. Iqbal, Effect of Ho^{3+} ions on microwave losses and hightemperature electrical behavior of Li-based magnetic oxides. Ceram. Int. **47**, 4633–4642 (2021)

42. E.E. Ateia, M.A. Ateia, M.M. Arman, Assessing of channel structure and magnetic properties on heavy metal ions removal from water. J. Mater. Sci.: Mater. Electron. **33**(11), 8958–8969 (2022)
43. H. Lueken, B.G. Magnetochemie, *Teubner Stuttgart* (B. G. Teubner, Leipzig, 1999)
44. R.D. Shannon, Revised effective ionic radii and systematic studies of interatomic distances in halides and chalcogenides. Acta Crystallogr Sect A Cryst Phys Diffr Theor Gener Crystallogr **32**(5), 751–767 (1976)
45. E. Dagotto, T. Hotta, A. Moreo, Colossal magnetoresistant materials: the key role of phase separation. Phys. Rep. **344**(1–3), 1–153 (2001)
46. A. Urushibara, Y. Moritomo, T. Arima, A. Asamitsu, G. Kido, Y. Tokura, Insulator-metal transition and giant magnetoresistance in $La_{1-x}Sr_xMnO_3$. Phys. Rev. B **51**(20), 14103 (1995)
47 A. Kumar, K.L. Yadav, J. Rani, Low temperature step magnetization and magnetodielectric study in $Bi_{0.95}La_{0.05}Fe_{1-x}Zr_xO_3$ ceramics. Mater. Chem. Phys. **134**(1), 430–434 (2012)
48. S. Sharif, G. Murtaza, T. Meydan, P.I. Williams, J. Cuenca, S.H. Hashimdeen, F. Shaheen, R. Ahmad, Structural, surface morphology, dielectric and magnetic properties of holmium doped $BiFeO_3$ thin films prepared by pulsed laser deposition. Thin Solid Films **662**, 83–89 (2018)
49. M.K. Ahmed, R. Ramadan, M. Afifi, A.A. Menazea, Au-doped carbonated hydroxyapatite sputtered on alumina scaffolds via pulsed laser deposition for biomedical applications. J. Mark. Res. **9**(4), 8854–8866 (2020)
50. X. Liu, R. Ma, X. Wang, Y. Ma, Y. Yang, L. Zhuang, S. Zhang, R. Jehan, J. Chen, X. Wang, Graphene oxide-based materials for efficient removal of heavy metal ions from aqueous solution: a review. Environ. Pollut. **252**, 62–73 (2019)
51. Q. Liu, Y. Liu, Distribution of Pb(II) species in aqueous solutions. J. Colloid Interface Sci. **268**(1), 266–269 (2003)
52. T.M. Elmorsi, Equilibrium isotherms and kinetic studies of removal of methylene blue dye by adsorption onto miswak leaves as a natural adsorbent. J. Environ. Prot. **2**(06), 817 (2011)